Susceptibility of microseismic triggering to small sinusoidal stress perturbations at the laboratory scale

Martin Colledge[1,2], Jérôme Aubry[1,2], Kristel Chanard[3], François Pétrélis[4], Clara Duverger[2], Laurent Bollinger[2]and Alexandre Schubnel[1]

[1]Laboratoire de Géologie, École Normale Supérieure, PSL University, CNRS,Paris, France
[2]CEA, DAM, DIF, Bruyères-le-Châtel, France
[3]Université Paris-Cité, Institut de physique du globe de Paris, CNRS, IGN, Paris, France
[4]Laboratoire de Physique de l'Ecole normale supérieure, ENS, PSL University, CNRS, Sorbonne Université, Université Paris-Diderot - Paris, France

Key Points:

- The response amplitude of acoustic emissions is proportional to the amplitude of the stress oscillations
- The response amplitude of acoustic emissions increases with both oscillation period and background loading rate
- The Gutenberg-Richter b-value is modulated by stress oscillations

Corresponding author: Martin Colledge, colledge@geologie.ens.fr

Abstract

Small transient stress perturbations are prone to trigger (micro)seismicity. In the Earth's crust, these stress perturbations can be caused by various sources such as the passage of seismic waves, forcing by tides, or hydrological seasonal loads. A better understanding of the dynamic of earthquake triggering by stress perturbations is essential in order to improve our understanding of earthquake physics and our consideration of seismic hazard. Here, we study an experimental sandstone-gouge-filled fault system undergoing combined far field loading and periodic stress perturbations (of variable amplitude and frequency) at crustal pressure conditions. Microseismicity — in the form of acoustic emissions (AE) — strains, and stresses, are continuously recorded in order to study the response of microseismicity as a function of loading rate, amplitude and frequency of a periodic stress perturbation. The observed AE distributions do not follow the predictions of a Coulomb failure model taking into account both constant loading and oscillation-induced strain rates. A susceptibility of the system's AE response to confinement pressure amplitude is estimated, which showcases a linear relation between confinement pressure amplitude and the AE response amplitude, observations which agree with recent higher frequency experimental results on dynamic triggering. The magnitude-frequency distribution of AEs is also computed. Oscillations in Gutenberg-Richter b-value are observed on experiment catalogues but are not quantified. Our experiments may help complement our understanding of the influence of low inertia stress phenomena on the distribution of seismicity, such as observations of dynamic triggering and seismicity modulation by solid earth tides or seasonal loading.

Plain Language Summary

Stresses exerted on faults are constantly subjected to fluctuations related to the periodicity of external forces applied to the Earth's crust, e.g., tidal forces, or seasonal variations in water loads. These stress variations have been linked to time periods when earthquakes are more likely to occur in some specific contexts, but the precise mechanisms at play are not fully understood. Experimental work is here conducted to examine the influence of several key parameters, namely oscillation period and amplitude and background tectonic velocity, on the occurrence of laboratory-scale microseismicity. Microseismicity periodicity is proportional to the stress oscillation amplitude, and both short oscillation period and low tectonic velocity cause microseismicity to correlate less with the stress oscillations, possibly explaining why short-period tides do not correlate well with seismicity whereas long-periods seasonal variations in stress have been shown to correlate with seismicity. The ratio between small and large events also appears to correlate with the stress oscillation, suggesting that stress oscillations might create conditions during which large events are more likely to occur.

1 Introduction

Earthquakes originate from the sudden release of elastic stresses on faults. These stresses are primarily built-up by tectonic processes over long periods of time. However, transient and oscillatory stress phenomena such as tidal, hydrological or dynamic loading due to seismic wave propagation also contribute to stressing faults. The existence of these stresses leads to the question of their role on earthquake nucleation and triggering. This question has historically been debated (e.g., Schuster, 1897; Davison, 1938; Klein, 1976; Heaton, 1982; Hartzell & Heaton, 1989), with a number of studies claiming either the existence or the absence of evidence of seismic periodicities at timescales corresponding to the invoked phenomena, with statistical limitations due to catalogue sizes, selection, and biases keeping the question from being settled. Recent rigorous studies have highlighted the existence of periodic variations in seismicity rates in various tectonic settings, such as annual variations of seismicity in continental collision zones such

as the Himalayas (Bollinger et al., 2007; Bettinelli et al., 2008; Ader & Avouac, 2013), in faults located near subduction zones as in Taiwan (Hsu et al., 2021) and Japan (Heki, 2003), in non-deforming intraplate region such as the New-Madrid Seismic Zone (Craig et al., 2017), and even in the case of deep-focus earthquakes (Zhan & Shearer, 2015). Observations of tidal variations of seismicity have also been made in shallow thrust faults (Cochran et al., 2004), as well as in seismicity associated with geothermal (Wang et al., 2022) and submarine volcanic activity (Tolstoy et al., 2002). Tidal forces have also been linked to the triggering of tectonic tremors (e.g., Rubinstein et al., 2008; Ide & Tanaka, 2014; Chen et al., 2018) and slow slips (Hawthorne & Rubin, 2010). Moreover, the dynamic triggering of earthquakes by transient oscillatory stress changes caused by seismic wave has largely been accepted (e.g., Hill et al., 1993; Anderson et al., 1994; Brodsky & van der Elst, 2014).

All these observations are difficult to interpret due to differences between studies, with significant changes in tectonic contexts, fault geometry, and oscillation frequency and amplitude. Theoretical and numerical studies have attempted to unify all these observations, invoking nucleation times relative to the period of the stress oscillations as one of the factor differentiating a stress controlled regime from a stressing rate controlled regime (Beeler & Lockner, 2003; Ader & Avouac, 2013; Heimisson & Avouac, 2020; Dublanchet, 2022), or suggesting magnitude-dependent and oscillation-geometry-dependent modulation (Pétrélis et al., 2021). Experimental studies focused on the links between stress oscillations and seismicity have investigated the increased synchronization of acoustic emissions temporal distribution with periodic stress oscillations prior to macroscopic failure (Chanard et al., 2019; Noël, Pimienta, & Violay, 2019) and either the triggering or the induced clock-advance of stick slips (Lockner & Beeler, 1999; Savage & Marone, 2007, 2008; Chelidze et al., 2010; Bartlow et al., 2012).

To the best of our knowledge, no studies have investigated the influence of stress oscillation parameters on acoustic emissions distributions in granular shear experiments, such that observations of seismicity modulation in different natural tectonic contexts lack experimental references. Furthering our understanding of the role of small periodic stress changes on earthquake triggering could have implications for earthquake hazard assessment. This has been highlighted by observations of magnitude-frequency distribution (b-value) variations due to tides (Ide et al., 2016) as well as by observations of gradually increased correlation of seismicity with tides prior to large megathrust earthquakes, which could signify that seismic response of faults close to failure grow more susceptible to stress variations (Tanaka, 2010, 2012). These latter observations have however been called into question for their statistical significance (Wang & Shearer, 2015) although experimental works lend credence to the soundness of the theory on which they are based(Chanard et al., 2019; Noël, Pimienta, & Violay, 2019). These elements act as further motivation to experimentally investigate the question.

In this study, we perform shearing experiments on a granular fault gouge analogue at different strain rates, in order to mimic different tectonic loading rates. Confinement pressure oscillations are applied and acoustic emissions within the gouge are monitored. The magnitude and phase of these acoustic emissions is then computed and analysed. We start by presenting our experimental set-up and the range of parameters explored within our study. We then present experimental results in the form of temporal distribution variations and magnitude properties of acoustic emissions. The modulation of the temporal distribution of the acoustic emissions is then quantified, and both the influence of the loading and oscillation parameters, and the variations of magnitude-frequency distributions with the stress oscillations are discussed. Finally, we consider an upscaled interpretation of our results and address their implications for seismology.

2 Experimental Setup

2.1 Material and Sample Preparation

Experiments were performed on matching aluminium cylindrical guide blocks 4 cm in diameter — referred herein as saw-cuts — on the saw-cuts' planar surfaces oriented 30° from the axial direction (Figure 1a). In order to mimic naturally occurring gouge-filled faults, we placed 20 grams of gouge — the equivalent of a roughly 5 mm thick layer — between the saw-cuts, which we enclosed with aluminium tape. The gouge was generated by crushing pieces of Fontainebleau sandstone — a well-studied sandstone known for its purity and its homogeneous composition of quartz grains of characteristic size 250 µm (Bourbie & Zinszner, 1985) — down to a fine polydisperse gouge, with the largest grain size matching the characteristic grain size (Figure 1b). The use of gouge to investigate microseismicity is not a novel idea The experiment was designed with an artificial fault with gouge to produce enough AEs for statistical significance of the AEs catalogue analysis, a criterion not met by experiments using bare rocks as fault analogues. The use of a gouge to investigate microseismicity experimentally is not a novel approach (e.g., Mair et al., 2007; P. A. Johnson et al., 2013).

Double component strain gauges (FCB-2-11, 120 Ω by Tokyo Sokki Kenkyujo Co., Ltd, Japan) were glued on each saw-cut to measure strain in both axial and radial directions. The saw-cuts were then inserted into a neoprene jacket. Eight acoustic transducers, consisting of a piezoelectric (PZT) crystal (PI CERAMIC PI255, 5 mm diameter, 2 mm thickness, 1 MHz central frequency) sensitive to P waves (normal to the sample-sensor surface) encased within a brass holder, were glued directly onto the upper guide block surface, in a wide formation depicted in Figure 1a. More information on the sensors can be found in Brantut et al. (2011). The array was designed such as to have a homogeneous coverage, with sensors as close as possible to the gouge layer in order to detect the smallest possible acoustic emissions. Finally, to ensure proper sealing from the pressurized oil present in the confining chamber, a bi-component epoxy resin was applied on the neoprene jacket around the holes punctured within the jacket for strain-gages and acoustic transducers inserts.

2.2 Experimental Setup

The sample is inserted into a triaxial apparatus at the École Normale Supérieure in Paris. One important feature of this experimental system is the presence of an auto-compensated confinement chamber, i.e., a chamber which counterbalances the confining pressure exerted on the piston. More details can be found in Schubnel et al. (2005). The auto-compensation process requires changes in the confining pressure to be gradual, as the pressure change needs a short amount of time to diffuse up to the compensation chamber. The piston displacement is measured with a Linear Variable Differential Transformer (LVDT) placed atop the piston with a $\sim 1\mu m$ resolution. Piston displacement, applied axial stress (σ_1), confining pressure (P_c), as well as differential stress ($\Delta\sigma = \sigma_1 - P_c$), radial and axial strains measured by strain gauges are recorded with a sampling rate of 10 Hz with a digital encoder (HBM MGC Plus). Resolution on acquired stresses is $\sim 10^{-3}$ MPa, on displacement 0.1μm and 10^{-6} on strains.

From these measurements, the shear and normal stress applied on the gouge plane of the sample can respectively be derived as

$$\tau = \frac{\Delta\sigma}{2}\sin(2\theta) \tag{1}$$

$$\sigma_N = \frac{\Delta\sigma}{2}(1+\cos(2\theta)) + P_c \tag{2}$$

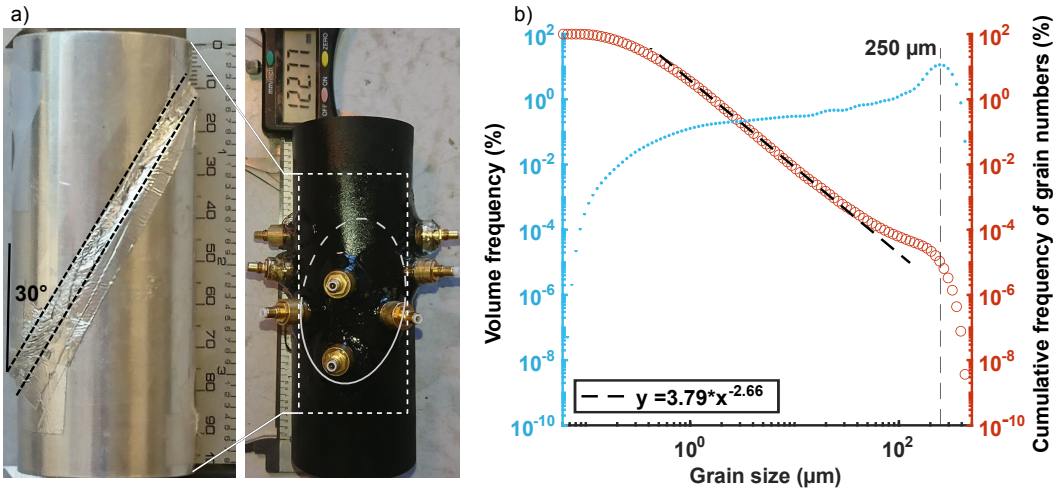

Figure 1. Sample Setup. (a) Post experiment saw-cuts with gouge cased in aluminium tape (left) and neoprene jacket with piezoceramic transducers (PZT) used as acoustic sensors (right). The ellipse indicates the fault location. (b) Cumulative frequency of grain size and volume frequency of grain size in the gouge. A close approximation of the power-law which the bulk of the distribution obeys is supplied. The characteristic grain size of 250 µm is overwhelmingly present in terms of volume, yet when considering the total number of grains only represents a small fraction of all grains.

where $\Delta\sigma$ is the differential stress, θ is the angle between the axial direction and the gouge plane (here $\theta = 30°$) and P_c is the confining pressure. The friction coefficient μ can thereafter be determined as,

$$\mu = \frac{\tau}{\sigma_N} \tag{3}$$

where τ and σ_N are the shear and normal stresses applied to the gouge layer. A change in the friction coefficient after a step in velocity, as displayed in Figure 2c depends on the $a - b$ parameter of the rate and state friction law:

$$\mu(\theta, V) = \mu_o + a \ln\left(\frac{V}{V_o}\right) + b \ln\left(\frac{V_o \theta}{D_c}\right) \tag{4}$$

where during a velocity change from V_o to V, μ, the friction coefficient, is a function of its reference value μ_o measured at V_o, the relative velocity increase, a state variable θ and the macroscopic critical slip distance D_c over which the friction coefficient reaches its new steady-state value. The fact that here $a - b > 0$ (2b) is important, as it demonstrates that the system is frictionally stable and ensures the absence of macroscopic stick-slip events (Marone, 1998). The absence of stick-slips reduces the clustering of the acoustic emissions catalogue into simple foreshock — mainshock — aftershock series, while allowing the presence of many smaller events, which lead to larger catalogues more suitable for statistical analysis. Finally, the fact that $a-b$ and D_c remain approximately constant throughout the test demonstrates that the system preserves its most important mechanical properties during the experiment. Whilst the gouge itself also undergoes strain, quantifying it precisely is not possible within our experiment. The gouge is therefore assumed to not undergo major changes in thickness after an initial compaction

regime visible in the first steps of our experiment (Figure 2a), both the friction coefficient and the acoustic emission rate reaching a plateau.

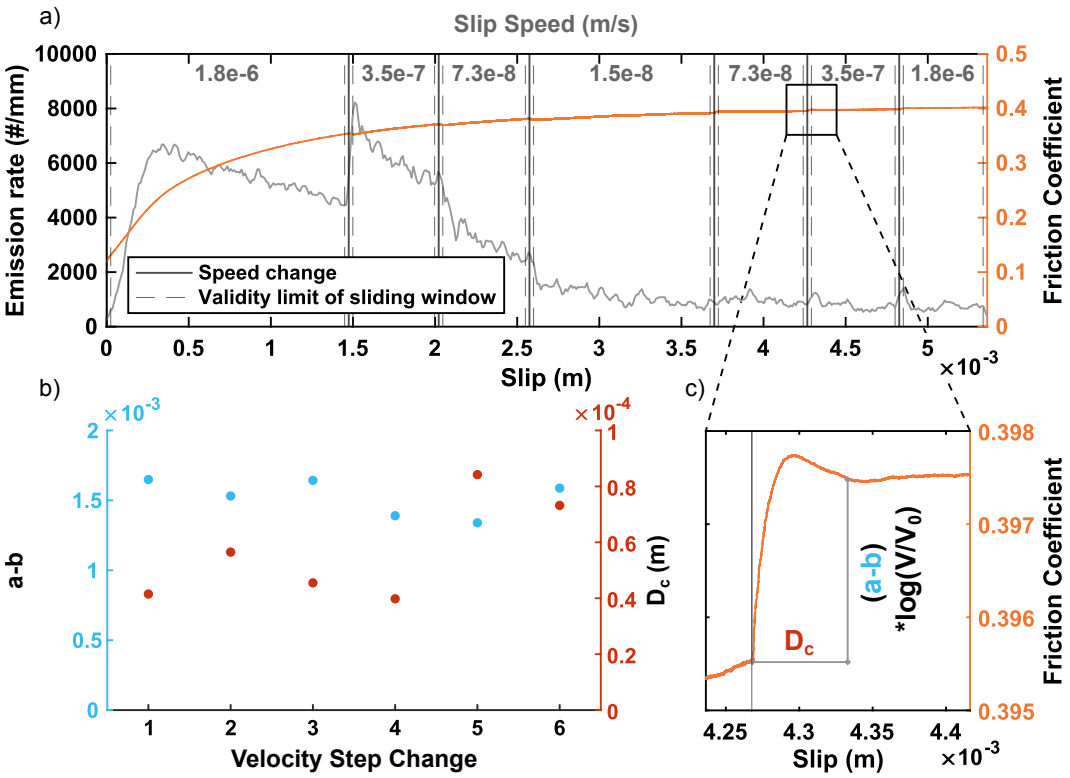

Figure 2. Control experiment mechanical parameters. (a) Friction coefficient and acoustic emission rate over a sliding window of $5*10^{-5}$ m of slip during the experiment. The last step is twice shorter than in following experiments. (b) Rate and state $a - b$ and D_c parameters as estimated from the control experiments at subsequent velocity changes. (c) The rate and state parameter a-b corresponds to the non-transient change of friction coefficient at a velocity change. D_c is the macroscopic length of the friction coefficient transient state at a velocity change.

Throughout the experiments, the piston and aluminium saw-cuts undergo elastic shortening. Thus, the measure given by the LVDT as the piston descends does not correspond to the actual slip occurring on the gouge plane. Slip δ is determined by correcting for the elastic contributions of both the machine and the saw-cuts as:

$$\delta = \left(LVDT - kF - \frac{\Delta\sigma}{E_{al}}L\right)\cos\theta \tag{5}$$

where $LVDT$ is the raw measure of displacement measured on the top of the piston by the LVDT, k (m/N) is the machine compliance, F is the applied load (equal to $F = \Delta\sigma\pi r^2$, with r the sample radius), L and E_{al} the aluminium sample length and Young's modulus respectively and finally θ the angle between the axial direction and the gouge plane.

2.3 Experimental Procedure

Once sealed inside the confinement chamber, the confining pressure exerted on the sample is raised to 90 MPa for several hours in order for the gouge to compact. During

Table 1. Experimental velocity steps details for all oscillation experiments.

Step Order	$\overline{V_p}^a$ (µm/s)	$\overline{V}$ (µm/s)	t_{step} (h:min)	d_p [b] (mm)
1	1.0	1.2±0.1	00:20	1.5
2	0.2	0.32±0.05	00:30	0.5
3	0.04	0.069±0.004	02:10	0.5
4	0.008	0.014±0.0003	22:10	1.0
5	0.04	0.074±0.003	02:10	0.5
6	0.2	0.37±0.03	00:30	0.5
7	1.0	1.9±0.1	00:12	1.0

[a] The difference in average slip velocity $\overline{V}$ for steps of identical injection rates are due to the elastic response of the saw-cuts and apparatus, which accommodates much of the displacement within the first steps. [b] The displacements d_p correspond to the LVDT measurements without correcting for the elastic deformation of the apparatus.

this stage, several thousands of acoustic emissions are detected, showcasing the effective compaction of the gouge via grain crushing and grain contact rearrangement. The confining pressure is then lowered to 50 MPa — corresponding to depths of approximately 2 km under typical lithostatic pressure conditions — for the rest of the duration of the experiment. The sample is then loaded uni-axially, the piston displacement being hydraulically servo-controlled via a high-pressure syringe pump. Displacement rate is controlled as a proxy by oil injection rate into the piston upper pressure chamber. A high injection rate step of 50 cc/h (i.e. corresponding to a piston velocity V of 1 μm/s) is first applied for 1.5 mm displacement, in order to elastically load the system, compact the gouge further and reach a frictional steady-state. The piston velocity is then lowered several times, by a factor of 5, to reach a minimum of approximately 10 nm/s. A displacement of 0.5 mm is allowed at each velocity step and the step duration t_{step} is therefore increased by a factor of 5 at each step (see Table 1). At each step, the slip velocity V is also computed. The piston displacement rate is then brought back up to its highest value by inverting velocity steps.

The slowest step, which lasts approxiimately a full day, is not repeated twice but is lengthened to insure the measured displacement during the step is twice that of faster steps.

In addition to a control experiment in which no oscillations are introduced, five experiments with different oscillation periods and amplitudes are conducted, as detailed in Tables 1 and 2. The investigated amplitudes correspond to 5%, 1% and 0.2% of the imposed confining pressure.

Stress modulations are performed by oscillating the confining pressure via a second servo-controlled hydraulic syringe pump. The oscillations are quasi-sinusoidal (by setting separately the amplitude, rate, acceleration and period of the pressure oscillation). Three important experimental limitations need to be pointed out here: 1) The confining pressure oscillations generate shear stress oscillations, albeit smaller, due to elastic couplings and to the geometry of the experimental setup; 2) Unfortunately, it is impossible with our system to perform confining pressure oscillations, while also maintaining it constant. In consequence, the experiments with oscillations were performed under "constant pressurized volume" conditions, which lead, because of oil leakage, to a slow linear confining pressure drop of $\sim$ 1.5MPa over the course of the experiments; 3) the period of oscillation is limited as a lower bound by the presence of an auto-compensation chamber, which precludes the investigation of very short periods. On the other hand, there exists an upper bound to the oscillation periods we could impose given our exper-

Table 2. Imposed oscillation parameters and acoustic emission statistics.

Exp #	ΔP_c (MPa)	T (s)	Acoustic Emissions
1	0.5	100	18152
2	0.1	100	15503
3	2.5	100	6358
4	0.5	20	19821
5	0.5	500	8742

imental procedure in order to allow multiple oscillation periods at the shorter experimental time steps.

Finally, the apparatus used to impose the stress oscillations does not produce oscillations of exactly the specified period. To improve the determination of the oscillation period, a Fourier Transform is applied to the confining pressure measurements. A Gaussian fit is then applied to the power spectrum in a frequency range surrounding the imposed period to determine the true oscillation period with improved precision (Gasior & Gonzalez, 2004). When the confining pressure measurements displays discontinuities due to erroneous values that require removing or to software restarts, the overall period is determined by taking an average of the thus derived periods weighed by the length of each segment. Calculations of the period over these segments give period estimate that are in good agreement with one another.

2.4 Acoustic Emissions Detection and Treatment

Acoustic emissions (AEs) are detected in triggering mode, i.e., by applying a voltage-threshold trigger logic, requiring at least 3 of the 8 acoustic sensors to reach a specified voltage (typically 100 mV, once amplified at 45dB - x150) within a given time window (typically 50 μs for waveforms to be recorded) . Waveforms of 8192 data points are recorded at 14bit, with a 10MHz sampling rate using an 8 channel digital oscilloscope. Recording, storage, management and basic data processing are performed using a licensed software (Insite, Applied Seismology Consulting Ltd.). The threshold trigger criteria were set so that the AE productivity rate remained below the maximum triggering rate capability ($\sim$ 50 AE/s) of the hardware throughout the experiment at least after the first velocity step.

Waveforms are first filtered with a two-pass low-pass filter of cut-off frequency 2 MHz in order to remove noise and better detect AEs. An STA/LTA auto-picking procedure is manually tuned to each sensor in each experiment after suppressing low signal-to-noise records to precisely determine the arrival time of the P-waves resulting from the AEs. In our catalogues, timing of AEs correspond to the P-picks arrival times as the travel times within the sample (less than 10 µs) are negligible compared to the imposed stress oscillations periods. Using the average Root Mean Square (RMS) of the AE waveforms, relative magnitudes M_r following Rivière et al. (2018):

$$M_r = log_{10}\left(\frac{\sum_1^n RMS}{n}\right) \tag{6}$$

with n the number of working AE sensors. Absolute magnitudes can also be determined by fitting, after careful sensor calibration (Marty, 2020), the average displacement spectrums for each AE using the Ω^{-2} law (Madariaga, 1976). Absolute magnitudes range roughly between -9 and -7 (Figure 3) and do not vary significantly in distribution across experiments. Comparing both magnitude estimates for each AE shows a good agree-

ment between magnitudes sets, both scaling linearly at the first order (Figure 3), thus verifying the validity and reliability of the absolute magnitudes. This is important as absolute magnitude could not be computed for all acoustic emissions due to numerical difficulties when fitting the Ω^{-2} law in a reliable manner on waveforms with poor signal to noise ratio. In the following, magnitude statistics are therefore computed using the RMS method, and assigning to relative magnitudes the corresponding absolute magnitude obtained by calibration and the Ω^{-2} law fitting.

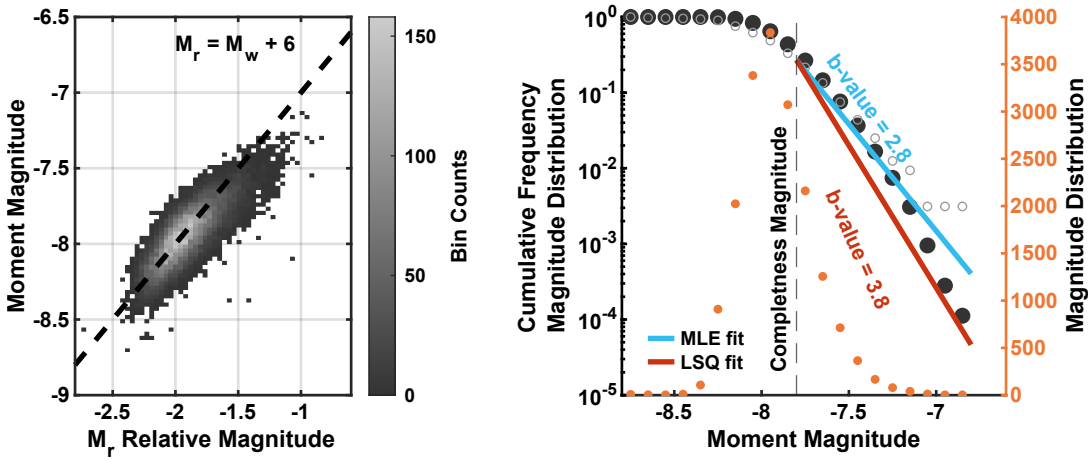

Figure 3. Magnitude distributions in experiment n°1. a) Absolute moment magnitudes against Root Mean Square (RMS) relative magnitudes. A line of slope 1 is provided for guidance to show that both magnitudes evaluation are in agreement and are linearly bound. b) Cumulative Frequency-Magnitude Distribution (FMD) of the RMS relative magnitudes (expressed as absolute moment magnitudes considering the relation derived in figure 3.a), for acoustic emissions for which the absolute magnitude was also calculated (closed black circles, N=17832 AEs), and for acoustic emissions for which it was not possible to determine the absolute magnitude (open grey circles, N=320 AEs). For other experiments, the amount of emissions for which the absolute magnitude could not be calculated can reach represent a significant portion of the AEs. The non-cumulative Magnitude Distribution of all events is also presented to illustrate the conservativeness of the completness magnitude estimate of -7.8. GR law fits obtained through the least-square method (red) and maximum likelihood estimations (blue) and using the events for which the absolute magnitude was calculated are also displayed. These are representative of all experiments.

3 Experimental Results

3.1 Acoustic Emission Rate and Mechanical properties

All stress modulation experiments demonstrate the same evolution in acoustic emission rate and friction as the control experiment (Figure 2). An initial compaction regime characterized by high AE rates and low friction coefficients progressively transitions into a stable regime with consistently low emission rates and high friction coefficients in the later steps.

The imposed stress oscillations induce fluctuations in the AE-rate (see subsection 3.2), slip velocity (Figure SI), friction coefficient, and shear and normal stress on the fault plane (Figures 2 and 4). The amplitude of the friction coefficient oscillations remain approximately constant throughout all velocity steps within an experiment. The amplitude

of the shear stress and normal stress oscillations however are highly dependent on the slip velocity and on the imposed stress oscillation parameters. Most notably, the shear stress oscillations are of the highest amplitude for the highest average slip velocities.

3.2 Acoustic Emission Temporal Distribution Relative to the Stress Oscillation

In order to determine whether discrete AEs are correlated with the applied stress oscillations over the many periods present in each velocity step, a coherent mean distribution of acoustic emissions is calculated by considering where each AE lies relative to the phase of the stress oscillation :

$$\phi \equiv \left(2\pi \frac{t - t_0}{T}\right) \mod 2\pi \tag{7}$$

where ϕ is the phase at which the AE occurs within the oscillation, t is the time at which the acoustic emission occurs, t_0 is the reference time of the oscillations defined as the time of a stress oscillation maximum, and T is the stress oscillation period.

As illustrated in Figure 4, AEs are not distributed uniformly over the stress oscillation but occur preferentially around specific phases, save for the lowest stress oscillation amplitude. This non-uniformity of the AE distributions is herein referred to as the modulation of the AE distribution. The influence of the oscillation amplitude on the distribution is greatly noted, the influence of the average slip velocity is also apparent. The higher the stress oscillation amplitude and the higher the average slip velocity, the more AEs are modulated. The influence of the period seems less significant.

3.3 Acoustic Emission Magnitudes

The magnitude distribution of AEs in laboratory experiments has repeatedly (e.g., Kiyoo, 1962; C. Scholz, 1968; Marty, 2020) been shown to follow the same distribution as earthquakes, i.e., the Gutenberg-Richter (GR) law:

$$N(M) = 10^{a-bM} \tag{8}$$

where N is the number of events of magnitude greater than M that occur, a and b being constants. The b-value of the GR-law describes the ratio of occurrence of large to small magnitude emissions and corresponds to the slope of the magnitude distribution above a certain cut-off magnitude M_c under which catalogues are deemed incomplete. The b-value is calculated using both a least-squares method and a maximum likelihood estimate (Aki, 1965), the latter being considered more accurate when estimating the b-value. Indeed, larger magnitude ranges are given less weight, thus accounting in some measure for the uncertainty linked to the small sample size of larger magnitude emissions. The b-values calculated in our experiments are relatively high, with little variation being noted from one experiment to the other.

The maximum likelihood estimations consistently yield smaller values between 2.8 and 3.3 whilst the least-square fits range between 3 and 4.5. This larger spread of b-values produced by the least-square method is expected due to its reliance on large emissions, of which the amount is highly variable due to the stochastic nature of AEs. Though rarely found associated with natural background seismicity of which b-values typically fall around 1, high b-values have been observed in seismic swarms (Adhikari et al., 2021) as well as in the presence of fluids (Murru et al., 1999; Bachmann et al., 2012). Such high b-values estimates could also in part be due to the relatively small dynamic range between the

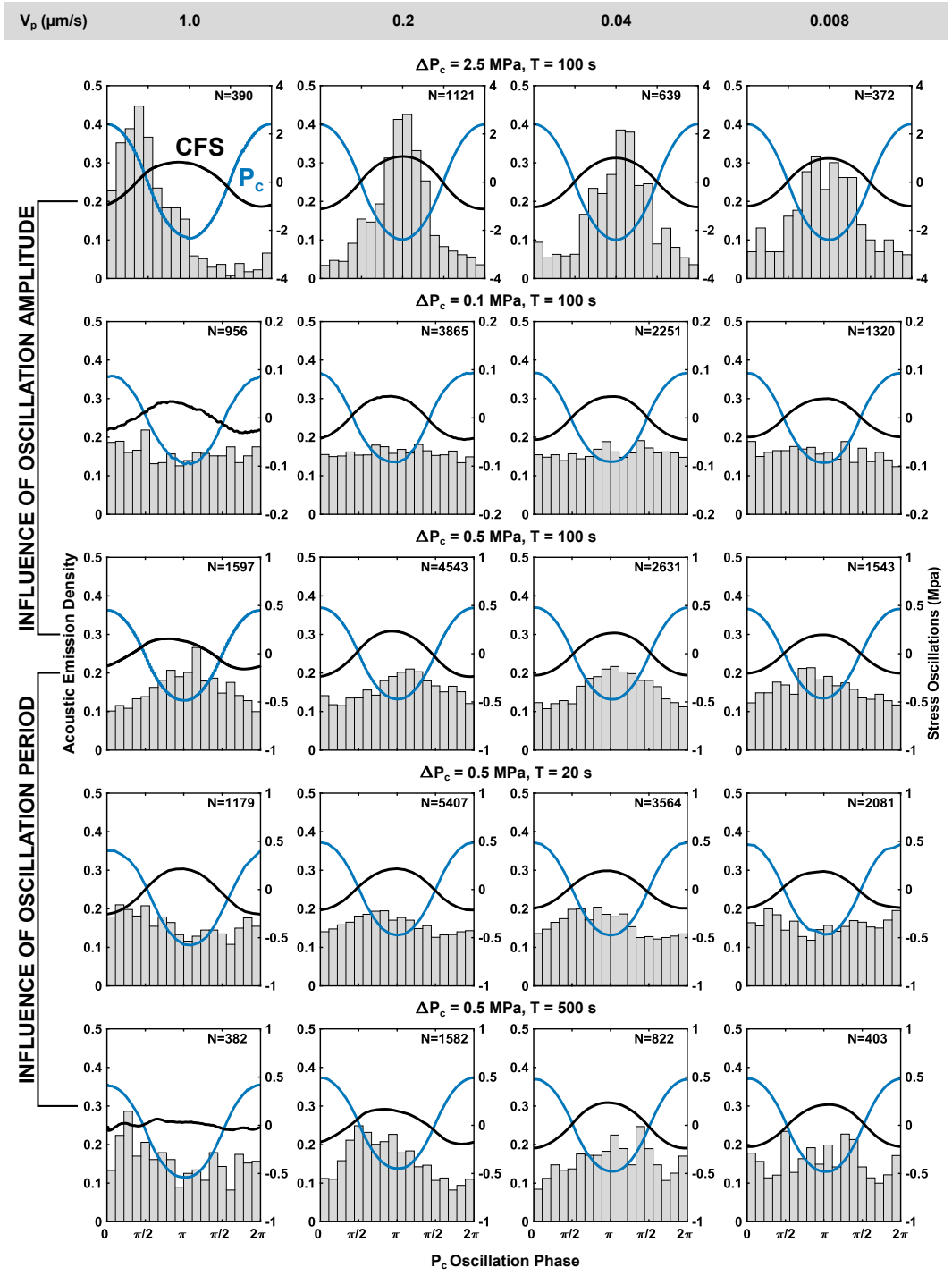

Figure 4. Acoustic emission phase distribution ($\phi = 0$ corresponds to the phase of maximum confining pressure), and detrended confining stress and Coulomb Failure stress perturbations at corresponding phases averaged over the velocity step. The velocity steps presented herein correspond to the the fused catalogues of AEs of steps of similar velocities, except for the 1µm/s step for which only the second step is presented as the first step corresponds to a transient state of the system wherein the gouge is not yet fully compacted. The graphs are disposed to illustrate the influence of oscillation amplitude, and the influence of the oscillation period.

completeness magnitude and the maximum magnitude which can cause overestimation of b-values as discussed in Marzocchi et al. (2020) and Geffers et al. (2022).

4 Discussion

4.1 Theoretical Coulomb Failure Model Framework

When considering the effect of periodic stress on seismicity modulation and triggering, Coulomb Failure stress is often times invoked (e.g. , C. W. Johnson et al., 2017; C. H. Scholz et al., 2019). Assuming a stable mechanical regime and according to (Knopoff, 1964) and (Beeler & Lockner, 2003), at oscillation periods larger than the nucleation time of microseismicty, Mohr-Coulomb theory should explain the distribution of the nucleation of microseismicity which should occur when specific stress thresholds are reached, whereas at oscillation periods smaller than the nucleation time, microseismicity should show reduced correlation with the oscillations. Within the context of the Coulomb Failure Model, assuming that these stress thresholds are on average uniformly spread out, the situation is equivalent to that of randomly spread out starting Coulomb stresses which lead to AEs when reaching a constant stress threshold. The constant background loading rate imposed on our sample induces a constant uniform stressing rate (Figure 5). Harmonic stress oscillations in turn induce harmonic oscillations in the stressing rate. In this theoretical framework, the phase distribution of events is controlled by a single parameter c:

$$c \propto \frac{\Delta S}{V\,T} \tag{9}$$

where ΔS is the Coulomb stress oscillation amplitude, V the loading rate and T the oscillation period. The parameter c is hereafter called the Coulomb stiffness because of its unit in MPa/m. If stress reversal, i.e., negative stress rate, occurs during the stress oscillation, the phases during which it occurs will exhibit quiescence, i.e., an absence of acoustic emissions, as the stress threshold will never be reached, thus preventing any nucleation from occurring. If the stress rate remains positive, however, the average theoretical distribution of AEs is sinusoidal. An important assumption made here is that the shear and normal stresses at a macroscopic scale apply at a microscopic scale.

Due to the complex geometry of our experimental system and to the oscillations of both normal and shear stresses on the fault, the notion of stress reversal relates to oscillations of the Coulomb failure stress defined as :

$$S = \tau - \mu' \sigma_N \tag{10}$$

where μ' is the static friction coefficient . Assuming $\mu' = 0.4$, a value close to that at which the effective friction coefficient arrives by the end of each of our experiments and comparable to that reported by the literature, the Coulomb stress oscillates and displays stress reversal at almost every velocity step, which is inline within the stress oscillation at short periods such as at tidal periods. The amplitude of the Coulomb stress oscillations is proportional to the amplitude of the imposed confining pressure such that $\Delta S = 0.4 \Delta P_c$. Therefore, the Coulomb control stiffness can be expressed as:

$$c \propto \frac{\Delta P_c}{V\,T} \tag{11}$$

This change allows the comparison with other experiments for which the Coulomb stress oscillation amplitudes is not known by using the imposed stress oscillation amplitudes. Some experiments also use imposed pore fluid pressure p_f oscillations. Considering constant values of shear and normal stress the resulting Coulomb stress oscillations are derived (Beeler et al., 2000), such that :

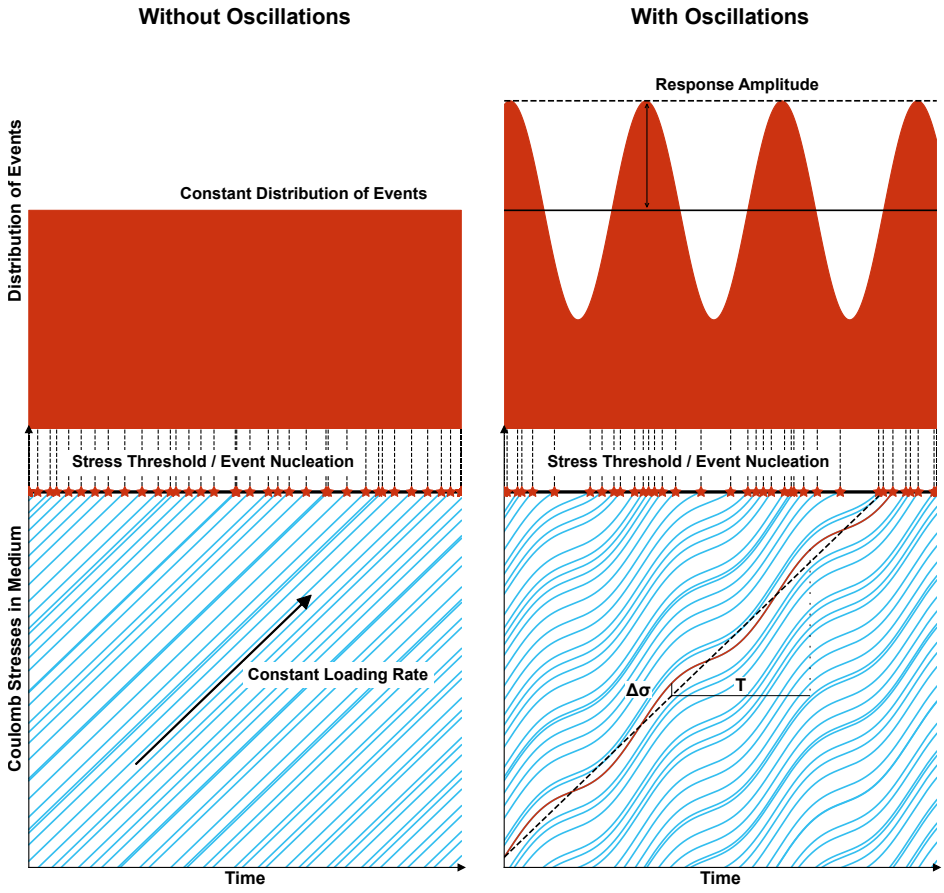

Figure 5. Coulomb Failure Model representation for acoustic emission triggering and associated modulation of acoustic emission distribution (modified from Beeler and Lockner (2003)). Coulomb stress is distributed randomly in the medium. A positive stress rate corresponding to a loading velocity V causes the Coulomb stress to increase throughout the medium. Once the Coulomb stress reaches a stress threshold the stress is released through an AE . Left : A constant loading rate results in a homogeneous distribution of events. Right : A modulation in the Coulomb stress (or stress rate) results in a modulation of the distribution of AEs.

$$\Delta S = \mu' \Delta p_f \tag{12}$$

Thus, considering a static friction coefficient of 0.4, the Coulomb stiffness can be generalized as:

$$c \propto \frac{\Delta\tilde{\sigma}}{V\,T} \tag{13}$$

with $\Delta\tilde{\sigma}$ the imposed stress oscillation amplitude.

The theoretical response amplitude directly correlates with the Coulomb stiffness, such that first order theoretical predictions can be derived :

1. For a given value of the Coulomb stiffness, regardless of stress reversal, the response amplitude should be constant;
2. The response amplitude increases with the Coulomb stiffness, regardless of stress reversal;
3. Quiescence should be observed whenever stress reversal is present.

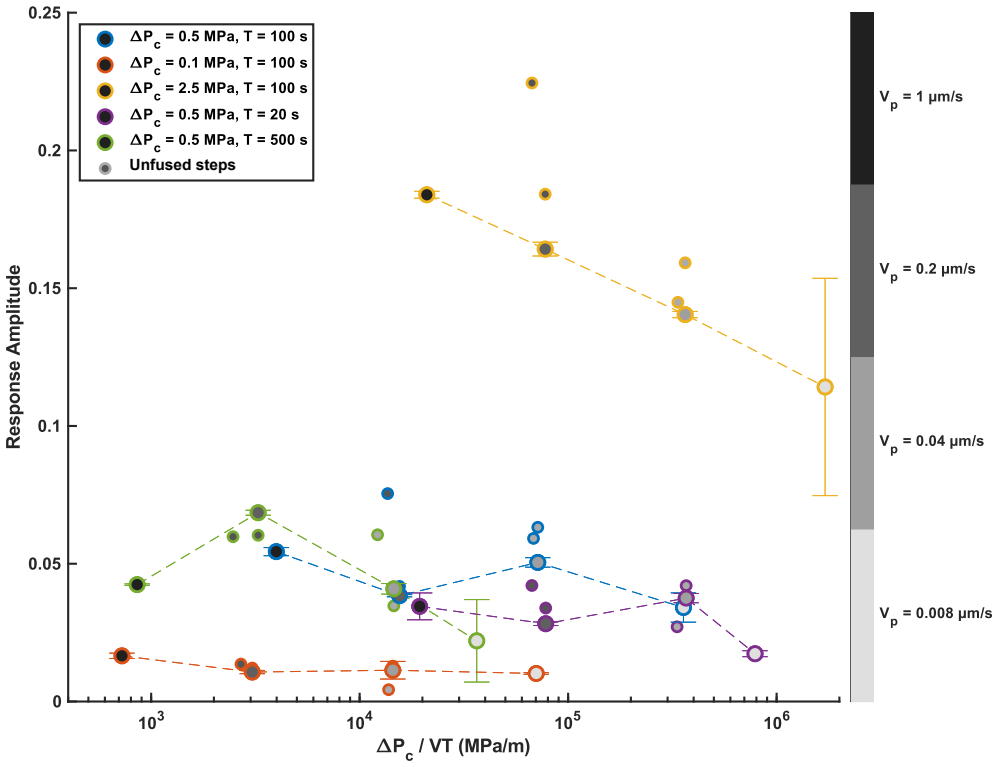

Figure 6. Response amplitude of the AE distribution at each velocity step as a function of the Coulomb stiffness. Small symbols correspond to the response amplitude of AE catalogues at each velocity step. Larger symbols linked by dashed lines correspond to the response amplitude of AE catalogues for which ascending and descending velocity steps were merged. Due to its transient nature, the very first step of each experiment is always excluded, thus the 1μm/s data points corresponds to the the final experimental step only. Error bars correspond to the standard deviation of the response amplitudes when calculated for AE catalogues divided into equal thirds, representative of each velocity.

Interestingly, our experimental results (Figure 6) do not match these predictions. The response amplitude is not directly correlated to the Coulomb stiffness, the influence of the stress oscillation amplitude being much greater than the influence of the oscillation period for instance, with increases in oscillation amplitude resulting in very large increases in response amplitude. Moreover, the influence of velocity is the opposite of the model prediction, as increasing velocity leads to increases in response amplitude. Finally, no consistent period of quiescence was observed in our AE distribution catalogues despite most of our experimental steps occurring under conditions of stress reversal. Moreover, the velocity steps where stress reversal occurs the most correspond to the lowest

velocity steps which also happen to be the steps where the response amplitude is at its lowest within each experiment. This implies that at lower velocities, the AE rate becomes oscillation-independent. This could be due to the complex geometry of the stress field within the gouge, stress oscillations may induce local stress heterogeneities which may promote nucleation during macroscopic stress reversals. At larger periods and slower velocities, greater visco-elastic relaxation of stress through creep may also take place. Such creep could in turn lead to increased background AE-rates that would also work against any shear stress build-up. This could also be due to the lower phase clustering of AEs at low velocities, which could allow less shear stress build-up throughout the oscillation (Figure 7). These observations could also signify that our experiments were mostly conducted in the high frequency regime described earlier.

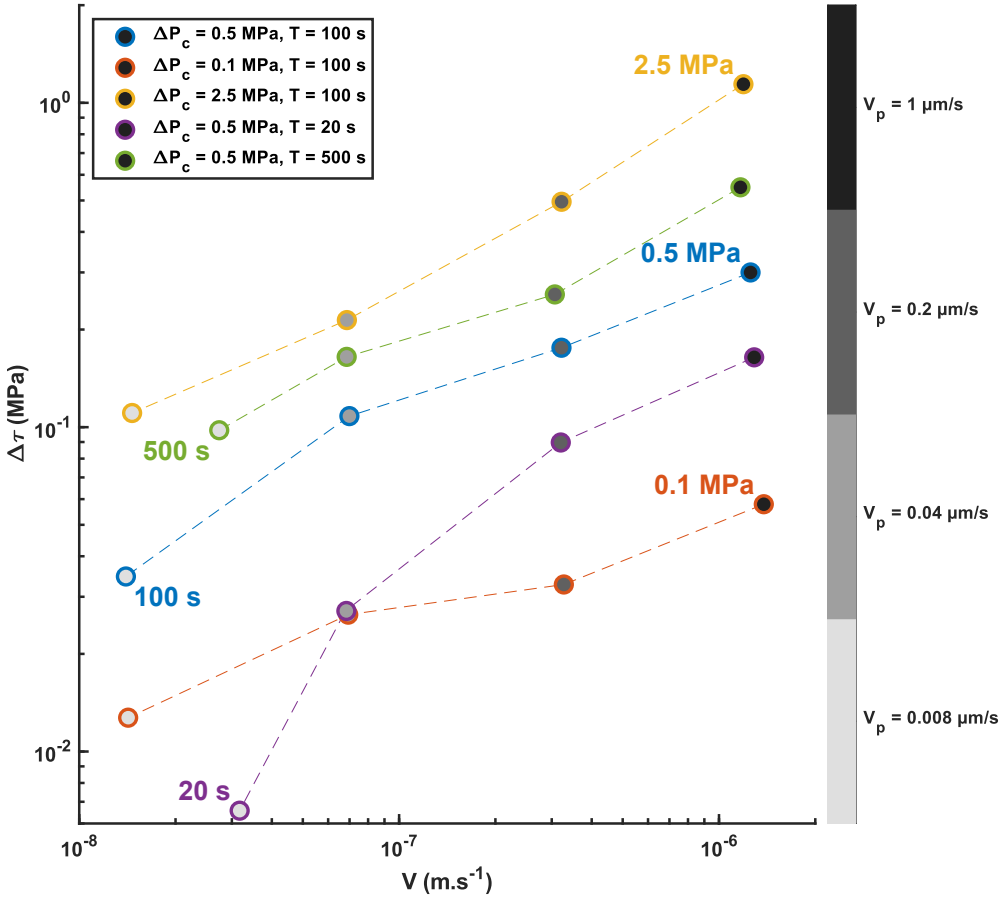

Figure 7. Evolution of the shear stress oscillation amplitude with slip velocity. Shear stress oscillation amplitude is derived by fitting the mean shear stress over one oscillation by a sinusoid of fixed period. The shear stress oscillation amplitude increases with velocity, and with both pressure oscillation amplitude and period, indicating that the imposed stress oscillations do not overall translate to equivalent shear stress oscillations on the fault plane.

This hypothesis is also supported by the phase of AEs. In most experimental steps, the preferential occurrence phase of AE correlates positively with the phase of greatest

Coulomb stress. This is in not in line with the Mohr-Coulomb failure mode which predicts that AEs should nucleate preferentially at phases of greatest stressing rate. The only steps for which such a correlation occurs are the highest velocity steps in the experiments with either the largest oscillation amplitude or the largest oscillation period. These results are in line with the theory of two nucleation-time-dependent regimes as initially described by Dieterich (1987). Both experimental (Beeler & Lockner, 2003) and numerical (Dublanchet, 2022) observations reproduce these behaviours. Likewise, our experiments straddle the line between the two nucleation regimes.

4.2 Susceptibility to Stress Oscillation Amplitude

Sinusoidal least-square fits of fixed periods of the AE phase histograms are calculated, the amplitudes of which are used as proxies for the response amplitude. For moderate stress oscillation amplitudes, numerical simulations (Pétrélis et al., 2021) observe a linear relation between the response amplitude and the oscillation amplitude such that:

$$s \propto \Delta\sigma \tag{14}$$

Calculating the susceptibility of the response amplitude to the confining pressure amplitude, i.e., the response amplitude divided by the stress oscillation amplitude,

$$\text{Susceptibility to } \Delta P_c = \frac{s}{\Delta P_c} \tag{15}$$

a collapse of our experimental data onto a single curve is observed when plotted against the Coulomb stiffness (Figure 8), confirming as a first-order approximation the linear scaling of the response amplitude with the oscillation amplitude.

Furthermore, data from studies involving competition between fluid-induced pore pressure oscillations and axial loading with different experimental conditions and setups to this study's (Chanard et al., 2019; Noël, Passelègue, et al., 2019; Noël, Pimienta, & Violay, 2019) follow the same trend when the susceptibility of their response amplitudes to the pore pressure oscillation amplitude is plotted against Coulomb stiffness. The response amplitude for these experiments was derived following the same procedure as for this study's experiments.

4.3 *b*-value modulation

The magnitude distribution of natural seismicity having been observed to be impacted by stress oscillations (Ide et al., 2016), an analysis of the maximum likelihood *b*-value variations was undertaken. In order to have large enough catalogues for *b*-value estimates to be statistically relevant, all acoustic emissions except those contained in the first 1mm of displacement of each experiment were here considered. AE sub-catalogues were divided for each experiment by selecting events that fell in a specified phase window, the width of which was either set to π or $\pi/2$ (Figure 9). This procedure was replicated by moving the phase window across the phase space.

Oscillations in b-value are observable regardless of the imposed phase window width for most experiments save for the lowest stress oscillation amplitude experiment (see SI). The amplitude of oscillation of the *b*-value increases with the stress oscillation amplitude, as observed in natural settings (e.g., C. H. Scholz, 2015; Tan et al., 2019). The effect of oscillation period on the b-value modulation, though a phase shifts between the different observed *b*-value oscillations could indicate a role of the oscillation period in the *b*-value oscillations.

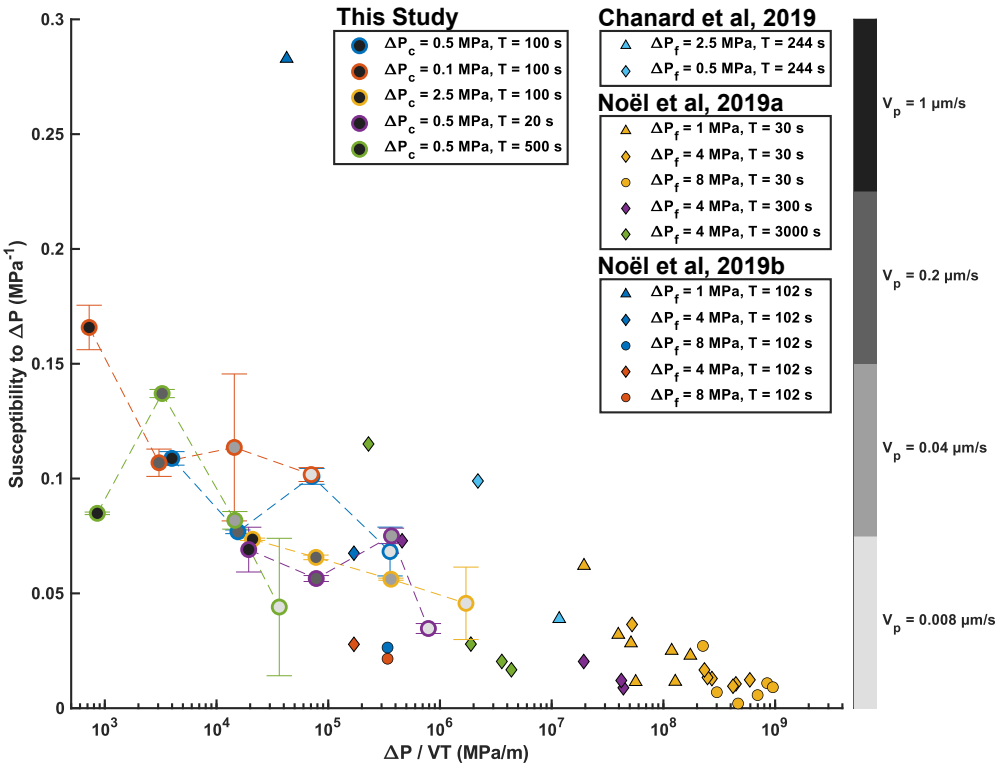

Figure 8. Susceptibility of the response amplitude of the AE distribution to the imposed stress oscillations amplitude (either pore pressure or confining pressure amplitude), as a function of the Coulomb Stiffness. Experimental results using data from Chanard et al. (2019), Noël, Passelègue, et al. (2019), and Noël, Pimienta, and Violay (2019), are also presented.

The width of this window has an influence on the observed oscillation b-value and on the uncertainties associated to them. Larger phase windows reduce uncertainty linked to the b-value estimation due to the increased number of AEs considered when computing them, thus also reducing the uncertainty linked to the oscillation of the b-value.

4.4 Relevance to natural oscillatory stress phenomena

Our experimental observations show an increase of microseismicity modulation primarily with increased stress oscillation amplitude as well as with both oscillation period and background loading rate. The increase of modulation with stressing amplitude is in line with the natural case, where seismicity has robustly been shown to be triggered by large stress variations caused by seismic wave propagation (Brodsky & van der Elst, 2014), and more modestly modulated at longer periods by smaller amplitude of stress variations (e.g., Bollinger et al., 2007; Métivier et al., 2009). Moreover, the increase of modulation with loading period could explain why despite tidal and seasonal or multi-annual stressing being of comparable amplitudes, tidal modulation is less commonly observed than seasonal and multi-annual modulation. Interestingly, our experimental results also show the role of background loading rates in modulating seismicity which seems consistent with larger scale observations. Indeed, natural faults appear to express different levels of sensitivity to oscillating stresses, for example at seasonal periods with the best con-

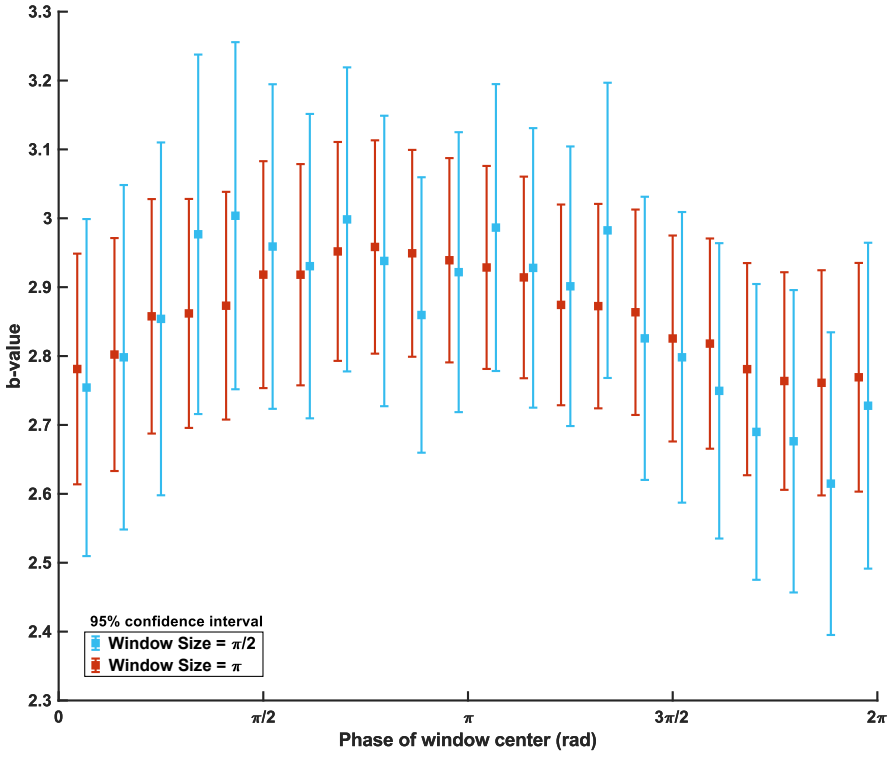

Figure 9. Gutenberg-Richter b-value in experiment n°1 calculated for AEs within a moving phase window of π (red) or $\pi/2$ (blue) throughout the experiment. The b-value is determined with a maximum likelihood estimate.

strained modulations being witnessed in tectonic contexts with large strain rates such as the Himalayas (Bollinger et al., 2007) or Alaska (C. W. Johnson et al., 2020). In fact, similarly to experimental results, natural observations of triggered or modulated seismicity by various transient and oscillatory phenomena can be represented by the Coulomb stiffness as a function of the oscillation period, covering more than 10 orders of magnitudes (Figure 10). Within this framework, natural observations and experimental results of this study roughly fall in a range of constant $\Delta\sigma/V$, whereas previous experiments performed under creep conditions explored higher $\Delta\sigma/V$ ratios with little resemblance to natural phenomena. However, the scaling of these observations is to be considered with caution. Indeed, the largest tectonic loading rates correspond to highly seismogenic zones (Ide, 2013) which deliver larger seismic catalogues and thereby make them more studied. Additionally, the seasonal modulation of seismicity in the New Madrid Seismic Zone (Craig et al., 2017) remains a troubling observation, as regional Global Navigatio Satellite System (GNSS) observations do not indicate any large scale deformation (Craig & Calais, 2014), although the seismicity could be explained by the presence of localised stress on and around specific faults not captured by the sparse GNSS network.

Experiments also show that an increase in the GR b-value increase is correlated with an increase in stress oscillation amplitude, but experimental limitations preclude the quantification of a phase link between stress and b-value. Yet, this link is coherent with the few natural observations of b-value modulation by stress oscillations (C. H. Scholz, 2015; Tan et al., 2019). Given that larger magnitude events have larger nucleation times (Ohnaka, 2000), it would be expected that the response regime of earthquakes to stress

oscillations would be magnitude dependent. This is could explain the b-value variations with stress oscillations and is inline with observations in the natural case where differential stress variations are linked to the b-value.

Some limitations of our experiments include assuming a fault geometry which is akin to that of thrust faults, these being the faults on which the modulation of earthquakes by periodic loading seems to be the most readily observed (Cochran et al., 2004; Ide et al., 2016; C. W. Johnson et al., 2017). It would be of interest to also consider the case of strike-slip geometries in the laboratory with an appropriated experimental device, to explore their response to different stressing conditions. Another experimental limitation of this work is the use of oscillation periods corresponding to the range between dynamic triggering and tidal characteristic Coulomb stiffness. The large oscillation periods of most natural oscillatory stress phenomena make experimental work with those periods difficult.

Table 3. Considered range of parameters for oscillatory natural phenomena.

	El Niño Loading	Seasonal Loading	Tidal Loading[a]	Seismic Wave Loading
T	2 - 10 years	1 year	6 hours - 1 year	1 - 10 seconds
$max(\Delta\sigma)^b$	5 kPa	5 kPa	25 kPa	100 kPa

[a] Including both Solid-Earth tides and water-loading due to ocean tides. [b] Orders of magnitude of the stress oscillation amplitudes upper bounds from C. W. Johnson et al. (2020), Anderson et al. (1994), Cochran et al. (2004).

5 Conclusions

Experiments were conducted to determine the modulation of microseismicity by stress oscillations in tectonic contexts. The resulting response amplitude of the microseismicity distribution is linearly susceptible to oscillation amplitude and increases with velocity. Our results mostly do not conform to the low frequency Coulomb-failure regime, indicating that the considered oscillation periods are smaller than the nucleation times of microseismicity (here recorded in the form of acoustic emissions). The susceptibility to stress amplitude does however scale with the Coulomb stiffness. Moreover, we show that experimental results tend to follow the same Coulomb stiffness - Period scaling law as natural seismicity linked to oscillatory phenomena. We experimentally confirm the absence of quiescence during stress reversal, probably linked to complex stress heterogeneities and visco-elastic relaxations taking place in our granular fault gouge medium. We also confirm the possibility of small oscillatory perturbations modulating the b-value, which is relevant to observations of tide-based modulation of seismicity b-value (Ide et al., 2016). Further investigation of the influence of stress oscillations on b-value could be useful for earthquake hazard assessment, as well as more experimental work to assess the response of acoustic emissions in both the high-frequency nucleation-driven regime and low-frequency threshold driven regime. Finally, one important perspective of this work is to address the specific case of the response and susceptibility of a system undergoing stick-slip motion, for which the microseismicity might be clustered into foreshock-mainshock-aftershock sequences, in order to investigate further how the susceptibility evolves during the seismic cycle at the laboratory scale.

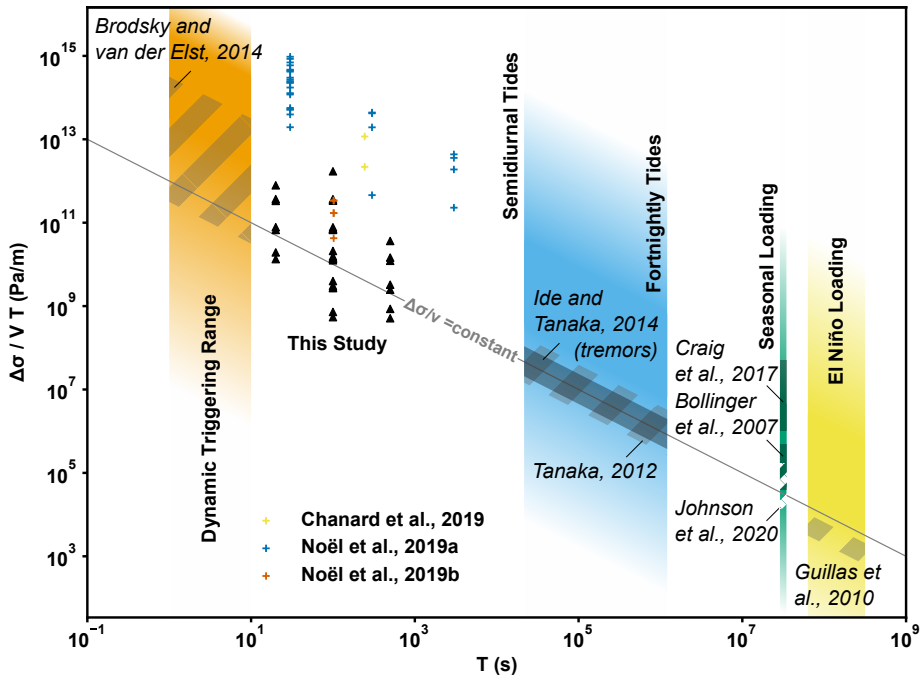

Figure 10. Coulomb stiffness as a function of oscillation period for experimental data and select natural seismicity observations from earthquake catalogues. In natural contexts with similar background stressing rates, stress oscillation of similar amplitudes but different periods elicit different response from seismogenic zones, e.g., directly or delayed triggered seismicity, modulation of seismicity rate, or no observed correlation. Velocities are taken from the references shown on the figure. Periods and stress variations are given in Table 3.

Acknowledgments

The authors would like to thank Takahiro HATANO, Julien GASC and Samson MARTY for valuable discussions and in the case of the two latter, for providing some of the pre-existing matlab codes that were used in this study. This work was supported by the LRC Yves Rocard (Laboratoire de Recherche Conventionné CEA-ENS-CNRS), the European Research Council grant #681346 REALISM and the Centre National de la Recherche Scientifique via the program 'Tellus-Aleas' of the Institut National des Sciences de l'Univers.

References

Ader, T. J., & Avouac, J.-P. (2013, September). Detecting periodicities and declustering in earthquake catalogs using the Schuster spectrum, application to Himalayan seismicity. *Earth and Planetary Science Letters*, *377–378*, 97–105. doi: 10.1016/j.epsl.2013.06.032

Adhikari, L. B., Bollinger, L., Vergne, J., Lambotte, S., Chanard, K., Laporte, M., ... et al. (2021). Orogenic collapse and stress adjustments revealed by an intense seismic swarm following the 2015 Gorkha earthquake in Nepal. *Frontiers in Earth Science*, 524.

Aki, K. (1965). Maximum likelihood estimate of b in the formula log N= a-bM and

its confidence limits. *Bull. Earthq. Res. Inst., Tokyo Univ.*, *43*, 237–239.

Anderson, J. G., Brune, J. N., Louie, J. N., Zeng, Y., Savage, M., Yu, G., ... de-Polo, D. (1994). Seismicity in the western Great Basin apparently triggered by the Landers, California, earthquake, 28 June 1992. *Bulletin of the Seismological Society of America*, *84*(3), 863–891.

Bachmann, C. E., Wiemer, S., Goertz-Allmann, B. P., & Woessner, J. (2012). Influence of pore-pressure on the event-size distribution of induced earthquakes. *Geophysical Research Letters*, *39*(9). doi: 10.1029/2012GL051480

Bartlow, N. M., Lockner, D. A., & Beeler, N. M. (2012). Laboratory triggering of stick-slip events by oscillatory loading in the presence of pore fluid with implications for physics of tectonic tremor. *Journal of Geophysical Research: Solid Earth*, *117*(B11). doi: 10.1029/2012JB009452

Beeler, N. M., & Lockner, D. A. (2003). Why earthquakes correlate weakly with the solid Earth tides: Effects of periodic stress on the rate and probability of earthquake occurrence. *Journal of Geophysical Research: Solid Earth*, *108*(B8).

Beeler, N. M., Simpson, R. W., Hickman, S. H., & Lockner, D. A. (2000, November). Pore fluid pressure, apparent friction, and Coulomb failure. *Journal of Geophysical Research: Solid Earth*, *105*(B11), 25533–25542. doi: 10.1029/2000JB900119

Bettinelli, P., Avouac, J.-P., Flouzat, M., Bollinger, L., Ramillien, G., Rajaure, S., & Sapkota, S. (2008, February). Seasonal variations of seismicity and geodetic strain in the Himalaya induced by surface hydrology. *Earth and Planetary Science Letters*, *266*(3-4), 332–344. doi: 10.1016/j.epsl.2007.11.021

Bollinger, L., Perrier, F., Avouac, J.-P., Sapkota, S., Gautam, U., & Tiwari, D. R. (2007). Seasonal modulation of seismicity in the Himalaya of Nepal. *Geophysical Research Letters*, *34*(8). doi: 10.1029/2006GL029192

Bourbie, T., & Zinszner, B. (1985). Hydraulic and acoustic properties as a function of porosity in Fontainebleau Sandstone. *Journal of Geophysical Research*, *90*(B13), 11524. doi: 10.1029/JB090iB13p11524

Brantut, N., Schubnel, A., & Guéguen, Y. (2011). Damage and rupture dynamics at the brittle-ductile transition: The case of gypsum. *Journal of Geophysical Research: Solid Earth*, *116*(B1).

Brodsky, E. E., & van der Elst, N. J. (2014). The uses of dynamic earthquake triggering. *Annual Review of Earth and Planetary Sciences*, *42*, 317–339.

Chanard, K., Nicolas, A., Hatano, T., Petrelis, F., Latour, S., Vinciguerra, S., & Schubnel, A. (2019, July). Sensitivity of Acoustic Emission Triggering to Small Pore Pressure Cycling Perturbations During Brittle Creep. *Geophysical Research Letters*, *46*(13), 7414–7423. doi: 10.1029/2019GL082093

Chelidze, T., Matcharashvili, T., Lursmanashvili, O., Varamashvili, N., Zhukova, N., & Meparidze, E. (2010). Triggering and synchronization of stick-slip: Experiments on spring-slider system. In *Synchronization and Triggering: From Fracture to Earthquake Processes* (pp. 123–164). Springer.

Chen, K. H., Tai, H.-J., Ide, S., Byrne, T. B., & Johnson, C. W. (2018). Tidal modulation and tectonic implications of tremors in Taiwan. *Journal of Geophysical Research: Solid Earth*, *123*(7), 5945–5964.

Cochran, E. S., Vidale, J. E., & Tanaka, S. (2004). Earth tides can trigger shallow thrust fault earthquakes. *Science*, *306*(5699), 1164–1166.

Craig, T. J., & Calais, E. (2014). Strain accumulation in the New Madrid and Wabash Valley seismic zones from 14 years of continuous GPS observation. *Journal of Geophysical Research: Solid Earth*, *119*(12), 9110–9129. doi: 10.1002/2014JB011498

Craig, T. J., Chanard, K., & Calais, E. (2017, December). Hydrologically-driven crustal stresses and seismicity in the New Madrid Seismic Zone. *Nature Communications*, *8*(1), 2143. doi: 10.1038/s41467-017-01696-w

Davison, C. (1938). *Studies on the Periodicity of Earthquakes.* T. Murby & Company, London.

Dieterich, J. H. (1987). Nucleation and triggering of earthquake slip: Effect of periodic stresses. *Tectonophysics*, *144*(1-3), 127–139.

Dublanchet, P. (2022). Seismicity modulation in a 3-D rate-and-state interacting fault population model. *Geophysical Journal International*, *229*(3), 1804–1823.

Gasior, M., & Gonzalez, J. (2004). *Improving FFT frequency measurement resolution by parabolic and gaussian interpolation* (Tech. Rep.). CERN-AB-Note-2004-021.

Geffers, G.-M., Main, I. G., & Naylor, M. (2022, June). Biases in estimating b-values from small earthquake catalogues: How high are high b-values? *Geophysical Journal International*, *229*(3), 1840–1855. doi: 10.1093/gji/ggac028

Hartzell, S., & Heaton, T. (1989). The fortnightly tide and the tidal triggering of earthquakes. *Bulletin of the Seismological Society of America*, *79*(4), 1282–1286.

Hawthorne, J. C., & Rubin, A. M. (2010). Tidal modulation of slow slip in Cascadia. *Journal of Geophysical Research: Solid Earth*, *115*(B9).

Heaton, T. H. (1982). Tidal triggering of earthquakes. *Bulletin of the Seismological Society of America*, *72*(6A), 2181–2200.

Heimisson, E., & Avouac, J.-P. (2020, November). Analytical Prediction of Seismicity Rate Due to Tides and Other Oscillating Stresses. *Geophysical Research Letters*, *47*. doi: 10.1029/2020GL090827

Heki, K. (2003, February). Snow load and seasonal variation of earthquake occurrence in Japan. *Earth and Planetary Science Letters*, *207*(1-4), 159–164. doi: 10.1016/S0012-821X(02)01148-2

Hill, D. P., Reasenberg, P., Michael, A., Arabaz, W., Beroza, G., Brumbaugh, D., ... et al. (1993). Seismicity remotely triggered by the magnitude 7.3 Landers, California, earthquake. *Science*, *260*(5114), 1617–1623.

Hsu, Y.-J., Kao, H., Bürgmann, R., Lee, Y.-T., Huang, H.-H., Hsu, Y.-F., ... Zhuang, J. (2021). Synchronized and asynchronous modulation of seismicity by hydrological loading: A case study in Taiwan. *Science advances*, *7*(16), eabf7282.

Ide, S. (2013, September). The proportionality between relative plate velocity and seismicity in subduction zones. *Nature Geoscience*, *6*(9), 780–784. doi: 10.1038/ngeo1901

Ide, S., & Tanaka, Y. (2014, June). Controls on plate motion by oscillating tidal stress: Evidence from deep tremors in western Japan: Ide et al.: Plate Motion by Tidal Stress. *Geophysical Research Letters*, *41*(11), 3842–3850. doi: 10.1002/2014GL060035

Ide, S., Yabe, S., & Tanaka, Y. (2016, November). Earthquake potential revealed by tidal influence on earthquake size–frequency statistics. *Nature Geoscience*, *9*(11), 834–837. doi: 10.1038/ngeo2796

Johnson, C. W., Fu, Y., & Bürgmann, R. (2017, June). Seasonal water storage, stress modulation, and California seismicity. *Science*, *356*(6343), 1161–1164. doi: 10.1126/science.aak9547

Johnson, C. W., Fu, Y., & Bürgmann, R. (2020). Hydrospheric modulation of stress and seismicity on shallow faults in southern Alaska. *Earth and Planetary Science Letters*, *530*, 115904.

Johnson, P. A., Ferdowsi, B., Kaproth, B. M., Scuderi, M., Griffa, M., Carmeliet, J., ... Marone, C. (2013). Acoustic emission and microslip precursors to stick-slip failure in sheared granular material. *Geophysical Research Letters*, *40*(21), 5627–5631.

Kiyoo, M. (1962). Study of elastic shocks caused by the fracture of heterogeneous materials and its relations to earthquake phenomena. *Bulletin of the Earth-*

quake Research Institute, University of Tokyo: Tokyo, Japan, 125–173.

Klein, F. W. (1976). Earthquake swarms and the semidiurnal solid earth tide. *Geophysical Journal International*, *45*(2), 245–295.

Knopoff, L. (1964). Earth tides as a triggering mechanism for earthquakes. *Bulletin of the Seismological Society of America*, *54*(6A), 1865–1870.

Lockner, D. A., & Beeler, N. M. (1999, September). Premonitory slip and tidal triggering of earthquakes. *Journal of Geophysical Research: Solid Earth*, *104*(B9), 20133–20151. doi: 10.1029/1999JB900205

Madariaga, R. (1976). Dynamics of an expanding circular fault. *Bulletin of the Seismological Society of America*, *66*(3), 639–666.

Mair, K., Marone, C., & Young, R. P. (2007). Rate dependence of acoustic emissions generated during shear of simulated fault gouge. *Bulletin of the seismological Society of America*, *97*(6), 1841–1849.

Marone, C. (1998). Laboratory-derived friction laws and their application to seismic faulting. *Annual Review of Earth and Planetary Sciences*, *26*(1), 643–696.

Marty, S. (2020). *High frequency radiation and foreshocks during laboratory earthquakes* (Unpublished doctoral dissertation). ENS, Paris.

Marzocchi, W., Spassiani, I., Stallone, A., & Taroni, M. (2020). How to be fooled searching for significant variations of the b-value. *Geophysical Journal International*, *220*(3), 1845–1856.

Métivier, L., de Viron, O., Conrad, C. P., Renault, S., Diament, M., & Patau, G. (2009, February). Evidence of earthquake triggering by the solid earth tides. *Earth and Planetary Science Letters*, *278*(3-4), 370–375. doi: 10.1016/j.epsl.2008.12.024

Murru, M., Montuori, C., Wyss, M., & Privitera, E. (1999). The locations of magma chambers at Mt. Etna, Italy, mapped by b-values. *Geophysical Research Letters*, *26*(16), 2553–2556. doi: 10.1029/1999GL900568

Noël, C., Passelègue, F. X., Giorgetti, C., & Violay, M. (2019). Fault Reactivation During Fluid Pressure Oscillations: Transition From Stable to Unstable Slip. *Journal of Geophysical Research: Solid Earth*, *124*(11), 10940–10953. doi: 10.1029/2019JB018517

Noël, C., Pimienta, L., & Violay, M. (2019, January). Time-Dependent Deformations of Sandstone During Pore Fluid Pressure Oscillations: Implications for Natural and Induced Seismicity. *Journal of Geophysical Research: Solid Earth*, *124*(1), 801–821. doi: 10.1029/2018JB016546

Ohnaka, M. (2000, December). A Physical Scaling Relation Between the Size of an Earthquake and its Nucleation Zone Size. *pure and applied geophysics*, *157*(11), 2259–2282. doi: 10.1007/PL00001084

Pétrélis, F., Chanard, K., Schubnel, A., & Hatano, T. (2021). Earthquake sensitivity to tides and seasons: Theoretical studies. *Journal of Statistical Mechanics: Theory and Experiment*, *2021*(2), 023404.

Rivière, J., Lv, Z., Johnson, P. A., & Marone, C. (2018, January). Evolution of b-value during the seismic cycle: Insights from laboratory experiments on simulated faults. *Earth and Planetary Science Letters*, *482*, 407–413. doi: 10.1016/j.epsl.2017.11.036

Rubinstein, J. L., La Rocca, M., Vidale, J. E., Creager, K. C., & Wech, A. G. (2008). Tidal modulation of nonvolcanic tremor. *Science*, *319*(5860), 186–189.

Savage, H. M., & Marone, C. (2007). Effects of shear velocity oscillations on stick-slip behavior in laboratory experiments. *Journal of Geophysical Research: Solid Earth*, *112*(B2).

Savage, H. M., & Marone, C. (2008). Potential for earthquake triggering from transient deformations. *Journal of Geophysical Research: Solid Earth*, *113*(B5).

Scholz, C. (1968). The frequency-magnitude relation of microfracturing in rock and its relation to earthquakes. *Bulletin of the seismological society of Amer-*

ica, *58*(1), 399–415.
Scholz, C. H. (2015). On the stress dependence of the earthquake b value. *Geophysical Research Letters*, *42*(5), 1399–1402. doi: 10.1002/2014GL062863
Scholz, C. H., Tan, Y. J., & Albino, F. (2019). The mechanism of tidal triggering of earthquakes at mid-ocean ridges. *Nature communications*, *10*(1), 1–7.
Schubnel, A., Fortin, J., Burlini, L., & Gueguen, Y. (2005). Damage and recovery of calcite rocks deformed in the cataclastic regime. *Geological Society, London, Special Publications*, *245*(1), 203–221.
Schuster, A. (1897). On lunar and solar periodicities of earthquakes. *Proceedings of the Royal Society of London*, *61*(369-377), 455–465.
Tan, Y. J., Waldhauser, F., Tolstoy, M., & Wilcock, W. S. D. (2019, April). Axial Seamount: Periodic tidal loading reveals stress dependence of the earthquake size distribution (b value). *Earth and Planetary Science Letters*, *512*, 39–45. doi: 10.1016/j.epsl.2019.01.047
Tanaka, S. (2010). Tidal triggering of earthquakes precursory to the recent Sumatra megathrust earthquakes of 26 December 2004 (Mw 9.0), 28 March 2005 (Mw 8.6), and 12 September 2007 (Mw 8.5). *Geophysical Research Letters*, *37*(2).
Tanaka, S. (2012). Tidal triggering of earthquakes prior to the 2011 Tohoku-Oki earthquake (Mw 9.1). *Geophysical research letters*, *39*(7).
Tolstoy, M., Vernon, F. L., Orcutt, J. A., & Wyatt, F. K. (2002). Breathing of the seafloor: Tidal correlations of seismicity at Axial volcano. *Geology*, *30*(6), 503–506.
Wang, W., & Shearer, P. M. (2015). No clear evidence for localized tidal periodicities in earthquakes in the central Japan region. *Journal of Geophysical Research: Solid Earth*, *120*(9), 6317–6328. doi: 10.1002/2015JB011937
Wang, W., Shearer, P. M., Vidale, J. E., Xu, X., Trugman, D. T., & Fialko, Y. (2022). Tidal modulation of seismicity at the Coso geothermal field. *Earth and Planetary Science Letters*, *579*, 117335.
Zhan, Z., & Shearer, P. M. (2015). Possible seasonality in large deep-focus earthquakes. *Geophysical Research Letters*, *42*(18), 7366–7373.